ELSEVIER

Contents lists available at ScienceDirect

Corrosion Science

journal homepage: www.elsevier.com/locate/corsci





Corrosion mechanisms in model binary metallic glass coatings on mild steel and correlation with electron work function

Chaitanya Mahajan ^a, Vahid Hasannaeimi ^a, Mayur Pole ^{a,1}, Elizabeth Kautz ^b, Bharat Gwalani ^c, Sundeep Mukherjee ^{a,*}

- a Department of Materials Science and Engineering, University of North Texas, Denton, TX 76203, USA
- ^b Energy and Environment Directorate, Pacific Northwest National Laboratory, Richland, WA 99352, USA
- ^c Physical and Computational Sciences Directorate, Pacific Northwest National Laboratory, Richland, WA 99352, USA

ARTICLE INFO

Keywords:
Metallic glass
Corrosion
Electrodeposition
X-ray photoelectron spectroscopy
Atom probe tomography
Scanning Kelvin probe

ABSTRACT

Effect of chemistry change on corrosion mechanisms and passive film characteristics of model Ni-P and Co-P metallic glass coatings on mild steel was studied because of their simple chemistry and widespread use. Increase in phosphorus content led to improved corrosion resistance. Results indicated the presence of hypophosphite and phosphate anions on the corroded surfaces. Enrichment of phosphorus in the passive layer was observed, which likely promoted the restoration of the protective hypophosphite anion layer during dissolution. A correlation between electronic structure and corrosion resistance was established, with relative work function increasing with increase in phosphorus content.

1. Introduction

Since first reported in 1960 [1], metallic glasses have undergone tremendous development over the past six decades [2-9]. The lack of long-range crystalline order in these materials results in remarkable properties, including ultra-high-strength, superior corrosion and wear resistance, and soft magnetism [10,11]. Metallic glasses may be thermo-plastically processed into complex shapes above their glass transition temperature, thereby combining the attractive properties of metals with the processing ease of polymers [12,13]. However, widespread use of metallic glasses has been restricted because of size limitations, high cooling rates necessary to achieve a fully amorphous structure, lack of plasticity, and catastrophic failure due to shear localization [14,15]. These restrictions may be overcome by the use of metallic glasses in the form of coatings and thin films [16] to take advantage of their outstanding surface properties without the associated limitations inherent in the bulk form. Many different routes have been utilized for the synthesis of amorphous coatings, including thermal spray [17], plasma sputtering [18], wire arc spraying [19], laser processing [20], and electrodeposition [21]. Electrodeposition represents a facile and scalable manufacturing toolbox with unique advantages, including fast deposition rate, low cost, no dilution effects from the

substrate, low operating temperatures, and tunability in terms of composition and achievable geometries [22]. Pulsed electrodeposition, which employs pulsed currents or potentials, further leads to a better quality of alloys with low defect density and greater versatility in terms of tuning their chemistry and properties [23].

Metallic glasses are attractive in corrosion applications because of their homogeneous and uniform microstructure free from crystalline defects, such as grain boundaries and phase boundaries, that are susceptible to preferential chemical attack [24]. However, this may be a "simplistic" interpretation, since the corrosion behavior of metallic glasses with a slight change in chemistry has been reported to be quite different [25]. An in-depth understanding of the role of metallic glass chemistry on their corrosion behavior requires systematic variation in composition using model alloy systems. In this regard, electrodeposition represents a versatile approach for achieving simple binary alloys in the amorphous form that is extremely difficult (if not impossible) to obtain by the conventional melt quenching route.

Here, we studied the corrosion behavior and passive film characteristics of $Ni_{100-x}P_x$ and $Co_{100-x}P_x$ electrodeposited metallic glasses (EMGs) with systematic variation in composition (x=5,10,15, and 20 at%). These two model alloy systems are of interest due to their magnetic and electrical characteristics [26,27], excellent corrosion and wear

E-mail address: sundeep.mukherjee@unt.edu (S. Mukherjee).

^{*} Corresponding author.

Current address: Physical and Computational Sciences Directorate, Pacific Northwest National Laboratory, Richland, WA, 99352, USA.

resistance [28,29], high hardness [22], and attractive functional properties [23]. They have also been proposed as effective diffusion barriers in microelectronic applications [30,31]. Ni-P shows good resistance to anodic dissolution in acids over the potential range where pure Ni actively dissolves [28]. The lower anodic dissolution of Ni-P has been attributed to the blocking action of phosphates [32], hypophosphite [33], phosphides [28], and elemental phosphorus [34], while other studies have shown limited passivation for Ni-P alloys [28,35]. Co-P alloys have been studied as a promising alternative to hexavalent-Cr plating because of their excellent chemical and mechanical properties as well as biocompatible nature [36]. However, there are no systematic studies on the corrosion behavior and passivation mechanisms of these model amorphous alloys as a function of composition. Furthermore, the role of electronic structure on the corrosion resistance and passive film characteristics of these metallic glasses is not well understood, which is critical in alloy design. Here, the corrosion response and surface binding energy were correlated with electron work function in both these technologically important alloy systems. In addition, X-ray photoelectron spectroscopy (XPS), transmission electron microscopy (TEM), and atom probe tomography (APT) were utilized to determine the characteristics of the surface passive film.

2. Experimental details

2.1. Electrodeposition process

Ni-P and Co-P alloys were obtained using pulsed reverse current (PRC) and pulsed current (PC) electrodeposition, respectively, using a pulse power supply (Dynatronix-MicroStar). The deposition parameters and bath composition for the two alloy systems are summarized in Table 1. The bath was prepared from analytical grade chemicals and was magnetically stirred at a rotation speed of 400 RPM for 24 h before deposition. Pure nickel and pure cobalt (99.99%) plates were used as soluble anodes and they were kept horizontally at 2 cm from the substrate. Mild steel (MS 1008) discs were used as cathode substrates and were mechanically polished to a 1 μm surface finish before deposition. A disc area of 2.83 cm² was exposed to the bath and the rest of the surface was masked with non-conductive paint. Before deposition, the polished substrates were ultrasonically cleaned in acetone for 10 min, followed by distilled water washing and subsequent chemical activation in 10 wt % HCl (2.74 M) for 30 s. The electrodeposition process was started

Table 1Electrodeposition parameters and bath composition for preparing Ni-P and Co-P alloys.

Composition	Quantity (g/ L)	Function
Ni-P Bath		
Nickel sulfate hexahydrate (NiSO ₄ 0.6 H ₂ O)	365	Nickel source
Phosphorus acid (H ₃ PO ₃)	32	Phosphorus source
Nickel chloride hexahydrate (NiCl ₂ 0.6 H ₂ O)	20	Conductive salt
Boric acid (H ₃ BO ₃)	40	pH buffer agent
Sodium dodecyl sulfate	0.4	Surfactant
$(NaC_{12}H_{25}SO_4)$		
pH	1.5 ± 0.1	
Temperature	37 ± 1 °C	
Agitation speed	90 RPM	
Co-P Bath		
Cobalt chloride (CoCl ₂)	25	Cobalt source
Sodium hypophosphite (NaH ₂ PO ₂)	20	Phosphorus source
Ammonium chloride (NH ₄ Cl)	20	Conductive salt & pH buffer
		agent
Saccharine (C ₇ H ₅ NO ₃ S)	0.3	Surfactant
pH	1.8 ± 0.1	
Temperature	$50\pm1~^{\circ}C$	
Agitation speed	250 RPM	

immediately after surface activation.

The cathodic current density was varied to obtain specific alloy chemistries (10, 15, and 20 at% of phosphorus). The phosphorus content decreased with increasing effective current density, indicating that phosphorus deposition proceeded via an indirect mechanism [37]. During the electrodeposition process, a Nernst diffusion layer is formed, affecting the kinetics between the center and edges of the substrate, resulting in non-uniformity of deposition [38,39]. The pulsed current (PC) and pulsed reverse current (PRC) increase the relaxation rate of the Nernst diffusion layer on the cathode surface, which decreases the composition and thickness variation across the surface. Uniform composition and thickness were obtained for the Ni-P alloys via PC waveform and for the Co-P alloys via PRC waveform. The rectangular waveforms of pulsed reverse current and pulsed current are shown in Fig. 1a. In the PC waveform, the variables are: (i) time on $(T_{ON} = 5 \text{ ms})$, (ii) time off ($T_{OFF} = 5$ ms), and (iii) forward current density ($J_F = 5$ –25 A/dm²). In the PRC, the waveform consists of the forward component and reverse component. The forward component consists of the forward time on $(T_{ON}^F = 5 \text{ ms})$, forward time off $(T_{OFF}^{\bar{F}} = 5 \text{ ms})$, total forward time (Forward = 10 ms), and forward current density ($J_F = 10-20 \text{ A/dm}^2$). While the reverse component is associated with the reverse time on (T_{ON}^R) = 2 ms), reverse time off ($T_{OFF}^{R} = 8$ ms), total reverse time ($T_{Reverse} = 10$ ms), and reverse current density ($J_R = 5 \text{ A/dm}^2$). The deposition time was set between 1 and 16 hr depending on the desired composition to obtain a thickness of ~ 35 –40 μm . Pure Ni and pure Co electrodeposition were done by removing the phosphorus source and using a cathodic current density of 15 A/dm² and pulsating current ($T_{ON} = T_{OFF} = 5$ ms). Fig. 1b shows an optical image of the electrodeposited samples with a systematic variation in phosphorus content for both the Ni- and Co-based systems.

2.2. Alloy characterization

2.2.1. Compositional and structural characterization

Coating thickness and elemental mapping along the cross-section of the deposits were done using FEI Quanta 200 scanning electron microscope (SEM) equipped with energy-dispersive X-ray spectroscopy (EDS). Crystal structure identification was done using high-resolution grazing angle X-ray diffraction (Rigaku Ultima III) with Cu-K α radiation ($\lambda=1.54$ Å) at a voltage of 20 kV.

2.2.2. Electrochemical measurements

The corrosion behavior of the alloys was studied using electrochemical impedance spectroscopy (EIS) and potentiodynamic polarization tests with a potentiostat/galvanostat (Reference 3000, Gamry) in a standard three-electrode cell. A standard calomel electrode was used as the reference and a graphite plate as the counter electrode. The corrosion experiments were performed in 3.5 wt% NaCl solution at room temperature. The samples were mechanically polished to 1200-grit paper. An area of 0.283 cm² was exposed to the solution using masking tape. The open-circuit potential (E_{OCP}) was measured for 1 h and found to be relatively stable for all the alloys. This was followed by EIS analysis at E_{OCP} over the frequency range of 0.01–100 kHz with a set AC voltage amplitude of 10 mV. The potentiodynamic polarization tests were carried out by scanning the specimen at a rate of 0.25 mV/s in the range of -250 mV (vs. E_{OCP}) to 1 V (vs. E_{OCP}). The corrosion rate (v_{corr}) was calculated as [40]:

$$v_{corr} = \frac{j_{corr} * K * EW}{\rho} \tag{1}$$

where, j_{corr} is the corrosion current density, $K = 3.27 \times 10^{-3}$ mm.g/(μ A. cm.year), EW is the equivalent weight. Equivalent weight (EW) is calculated as:

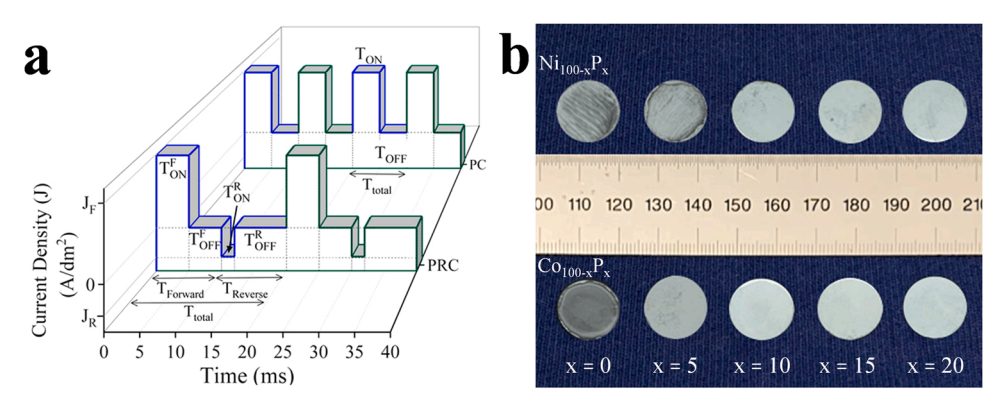


Fig. 1. (a) Pulsed reverse current (PRC) and pulsed current (PC) waveforms used in electrodeposition. In the PRC waveform, the forward time on (T_{ON}^F) , forward time off (T_{OFF}^F) , total forward time (forward), and forward current density (J_F) variables are associated with the forward current; the reverse time on (T_{ON}^R) , reverse time off (T_{OFF}^R) , total reverse time (reverse), and reverse current density (J_R) variables are associated with the reverse current. In the PC waveform, the variables are time on (T_{ON}) , time off (T_{OFF}) , and forward current density (J_F) ; (b) Optical image of the Ni-based and Co-based alloys with different compositions obtained by electrodeposition.

$$EW = \sum \left(\frac{n_i f_i}{W_i}\right) \tag{2}$$

where, f_i is the mass fraction, Wi is the atomic weight, and n_i is the valence of the ith element of the alloy.

2.2.3. X-ray photoelectron spectroscopy (XPS)

X-ray photoelectron spectroscopy (XPS-PHI 5000 Versaprobe) was performed to determine the nature of the passivation layer. The binding energies were calibrated based on the C 1 s peak value at 284.6 eV. The surface of the samples was analyzed after exposing them to the electrolyte at the open-circuit potential for 1 hr and different anodic polarization values. Prior to anodic polarization, the samples were exposed to the electrolyte at the open-circuit potential for 15 min, then polarized in the passive region ($E_{OCP} + 200 \text{ mV}$) for 1 hr and trans-passive region ($E_{OCP} + 600 \text{ mV}$) for 10 s

2.2.4. Transmission electron microscopy (TEM) and atom probe topography (APT)

 $Ni_{80}P_{20}$ samples were immersed in 3.5 wt% NaCl solution at open-circuit potential (as detailed in Section 2.2.2.) and then coated with \sim 20 nm Cr and \sim 50 nm Ni using an ion beam sputtering system prior to TEM and APT sample preparation. This Ni/Cr bilayer was used as a fiducial marker for determining the passive film-metal interface in the final TEM lamellae and APT needle apex [41]. TEM and APT samples were prepared using a FEI Helios dual-beam focused ion beam scanning electron microscope (FIB-SEM). The TEM lamellae and APT needles were prepared by depositing a Pt capping and extracting a cantilever from the sample including the base alloy, passive film, and Ni/Cr coating. Samples were prepared so that the Ni/Cr capping layer remained at the top surface of the TEM lamellae and APT needle apex.

Crystallographic characterization of the passive film and substrate was done with a probe-corrected FEI Titan 80–300 STEM instrument operated at 300 kV. The observations were performed using STEM with a high-angle annular dark-field (HAADF) detector. The probe convergence angle was 18 mrad and the inner detection angle on the HAADF detector was three times larger than the probe convergence angle.

A CAMECA local electrode atom probe (LEAP) 4000X HR system equipped with a 355 nm wavelength UV laser was used for APT data collection with the following user-selected parameters: 200 pJ/pulse laser energy, 125 kHz pulse repetition rate, 50 K specimen base temperature, and 0.003 detected ions/pulse detection rate. Data were reconstructed and analyzed using the Interactive Visualization and Analysis Software (IVAS), version 3.8.2 by CAMECA. Concentration across the capping layer/passive film/substrate interfaces was determined using a 1D concentration profile along the z-axis of a cylinder (15 nm diameter, 25 nm length), with a bin width of 0.2 nm.

2.2.5. Scanning Kelvin Probe (SKP)

A Scanning Kelvin Probe (SKP) microscope (Princeton Applied

Research) was used to measure the relative work function distribution over the surface. A tungsten probe with a perpendicular amplitude of 30 μ m with respect to the sample surface and frequency of 80 Hz was used as the reference probe during SKP measurements. The relative work function was determined at a tip-to sample distance of 50 μ m in lab air (RH 55%). SKP potential (V_{SKP}) is the potential applied by the instrument to nullify the existing contact potential between the tungsten probe and the sample surface. Therefore, it is a measure of the work function of the sample with respect to the tungsten probe (V_{SKP} = $\Phi_{Tungsten}$ - $\Phi_{Specimen}$). Considering the constant work function of the tungsten probe and identical ambient conditions for all the samples, the difference in potential values for the different samples was attributed to their relative electron work function.

3. Results and discussion

3.1. Compositional and Structural Characterization

Fig. 2(a & e) show the representative cross-section SEM images for $\text{Ni}_{80}\text{P}_{20}$ and $\text{Co}_{80}\text{P}_{20},$ respectively, on a mild steel substrate. The other compositions showed very similar characteristics with the uniform film thickness of 35 - 40 um, that was free from cracks and pores. Representative elemental maps are shown in Fig. 2(b-d) for Ni₈₀P₂₀ and Fig. 2 (f-h) for Co₈₀P₂₀, respectively, with composition variation across the interface of less than 0.5 at%. Fig. S1(a & b) shows the composition line profiles for Ni₈₀P₂₀ and Co₈₀P₂₀ EMGs, respectively. The elemental maps and line profiles indicate homogeneous distribution of the constituent elements. Fig. 2(i & j) shows the XRD patterns for Ni_{100-x}P_x and Co_{100-x}P_x electrodeposited alloys with systematic variation in composition (x = 0, 5, 10, 15,and 20 at%). Pure electrodeposited Ni showed a face-centered cubic (FCC) structure with (111), (200), and (220) peaks. Pure electrodeposited Co showed (100), (002), (101), and (110) peaks of hexagonal close-packed (HCP) structure. The Ni₉₅P₅ and Co₉₅P₅ alloys showed relatively broad (111) peaks indicating nanocrystalline microstructure. Amorphous alloy formation was seen for phosphorus content in the range of 10-20 at% in both the systems. Amorphous alloy formation for $M_{90}P_{10}$, $M_{85}P_{15}$, and $M_{80}P_{20}$, where "M" represents Ni or Co, may be attributed to the higher phosphorus content, which hindered crystal nucleation and surface diffusion of Ni and Co atoms during the concurrent deposition. The high overpotentials during electrodeposition lead to rapid discharge of atoms, making it difficult for them to attain their thermodynamically stable crystalline structure [42].

3.2. Electrochemical impedance spectroscopy (EIS)

Electrochemical impedance spectroscopy (EIS) measurements were employed for fundamental understanding of the capacitive behavior of surface passivation film for the EMGs in comparison with electrodeposited pure Ni, electrodeposited pure Co, and mild steel (MS 1008). The open-circuit potential (E_{OCP}) was measured for 1 h prior to EIS

C. Mahajan et al. Corrosion Science 207 (2022) 110578

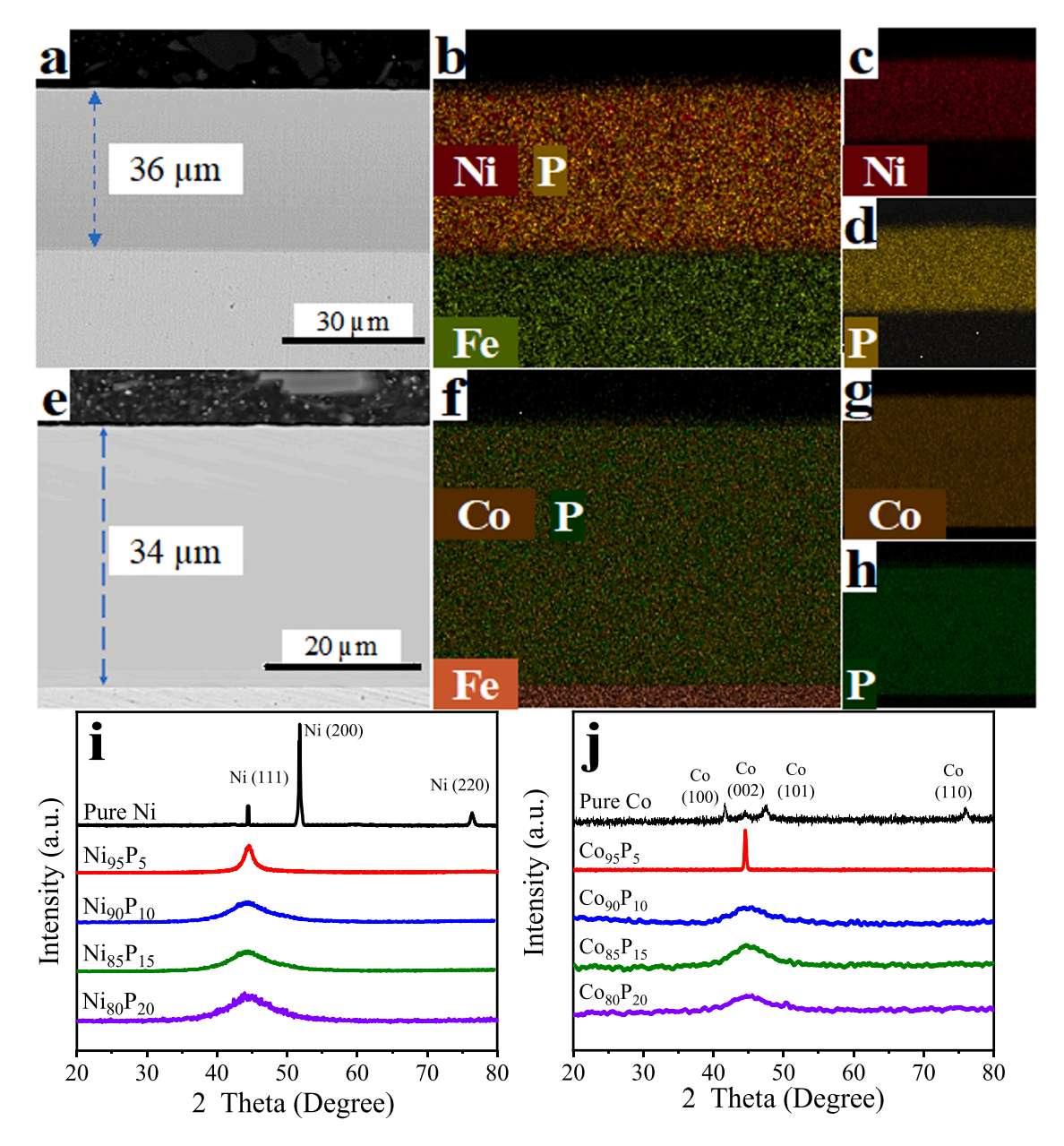


Fig. 2. (a) Cross-section SEM micrograph of $Ni_{80}P_{20}$ showing a thickness of $\sim 36\,\mu m$ and (b, c, d) elemental EDS maps for $Ni_{80}P_{20}$; (e) cross-sectional SEM micrograph of $Co_{80}P_{20}$ showing a thickness of $\sim 34\,\mu m$ and (f, g, h) elemental EDS maps for $Co_{80}P_{20}$; (i) XRD spectra of electrodeposited $Ni_{100-x}P_x$ (x = 0, 5, 10, 15, and 20 at%); (j) XRD spectra of electrodeposited $Co_{100-x}P_x$ (x = 0, 5, 10, 15, and 20 at%).

measurements and found to be relatively stable for all the alloys, EOCP values are summarized in Table S1. The Nyquist plots are shown in Fig. 3 (a & b). The Nyquist plots were close to a semi-circular arc in the investigated frequency range. The radius of the semi-circular arc increased with increase in phosphorus content, indicating that the surface passive film became more protective for higher metalloid fraction in the alloys. The corresponding Bode plots are shown in Fig. S2(a-d), where the phase angle varies between -70° to -85° , suggesting that the film is mainly capacitive [43]. At high frequency (> 10 K Hz), all the phase angles approached zero suggesting that the impedance was mainly determined by the pure solution resistance between the reference and working electrodes [44]. As the phosphorus content was increased in the coatings, the peak phase angle approached -90° indicating the formation of more stable and protective passive film. Phase angle curves for Ni₉₀P₁₀ and pure Ni showed two peaks between medium to high frequency, and MS1008 showed a second peak in the high frequency region (Fig. S2(c)). The peak in higher frequency range is attributed to porous passive layer and another in the lower frequency range is associated with charge transfer through the double layer [45–47]. The equivalent circuit of impedance spectra with two capacitive loops is shown in Fig. 3c. Ni $_{85}$ P1 $_{5}$, Ni $_{80}$ P2 $_{0}$, Co $_{90}$ P1 $_{0}$, Co $_{85}$ P1 $_{5}$, Co $_{80}$ P2 $_{0}$, and pure Co showed single extremums in the phase angle plots indicating the presence of one time constant, with the corresponding equivalent circuit shown in Fig. 3d. The equivalent circuits consisting of resistors and capacitors are shown in Fig. 3(c & d), which simulated the electrochemical behavior of the surface-solution interface. A constant phase element (CPE) was used to account for the non-ideal behavior of the double layer, like surface roughness, adsorption effects, and surface inhomogeneities, instead of pure capacitance [48,49]. CPE impedance may be represented as follows [50,51]:

$$Z_{CPE} = Y_0(j\omega)^{1-n} \tag{3}$$

where, Y_0 and n are the admittance constant and empirical exponent of the CPE, respectively, $j^2=-1$ and, ω is the angular frequency. The

C. Mahajan et al. Corrosion Science 207 (2022) 110578

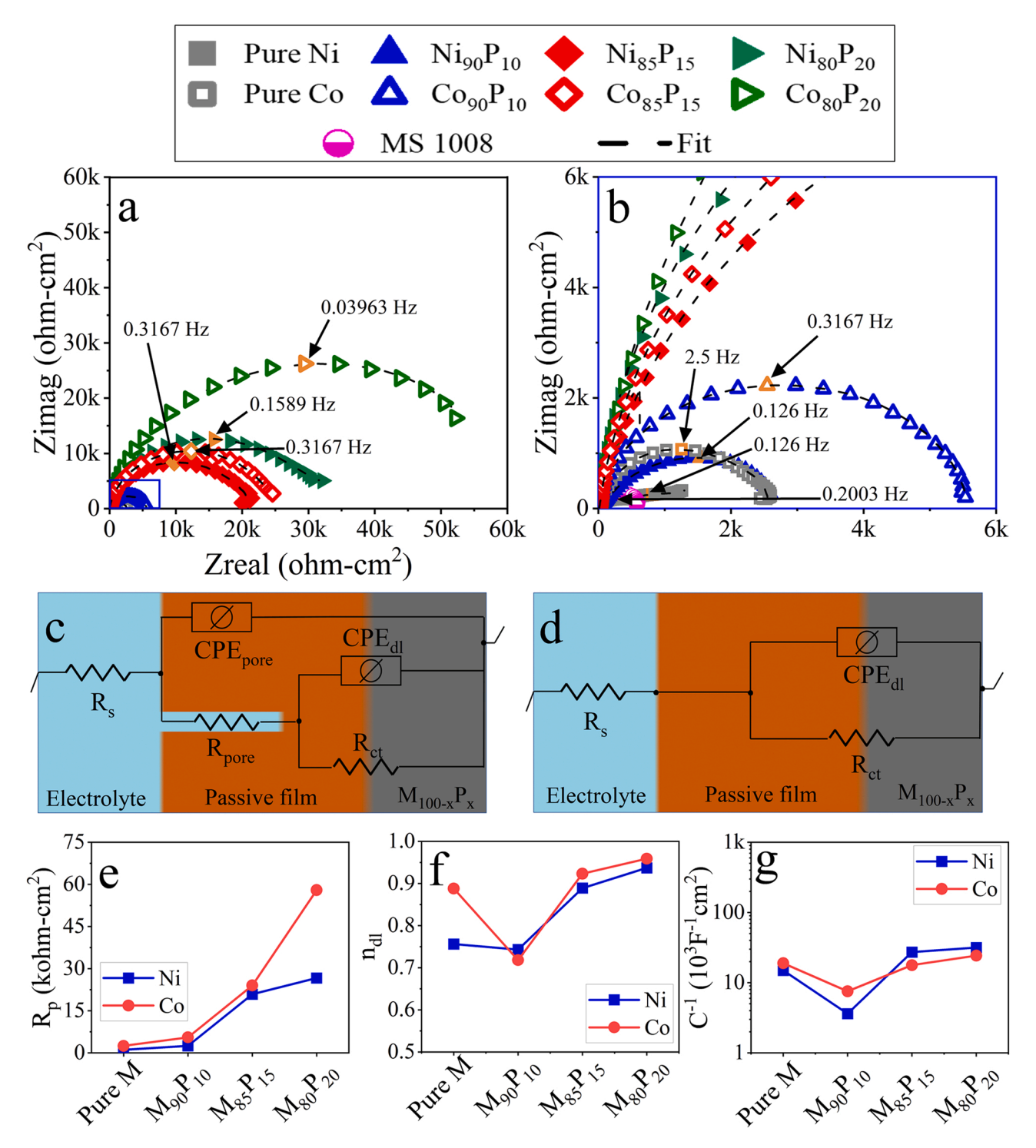


Fig. 3. EIS measurements: (a) EIS Nyquist plots for Ni-P, Co-P EMGs and the corresponding pure metals after 1 h of immersion in 3.5 wt% NaCl solution at their respective open-circuit potentials; (b) Zoomed in view of a section of part (a) showing the smaller capacitive loops, and the respective characteristic frequency (ω''_{max}) is shown by arrows; (c) two time-constant phase element circuit used for fitting the EIS data for pure Ni, Ni₉₀P₁₀, and MS 1008; (d) one time-constant phase element circuit used to fit Ni₈₅P₁₅, Ni₈₀P₂₀, pure Co, Co₉₀P₁₀, Co₈₅P₁₅, and Co₈₀P₂₀; (e) Polarization resistance (R_p), (f) CPE_{dl} exponent (n_{dl}), and (g) reciprocal of Capacitance (1/C) versus the phosphorus content in the EMGs and the corresponding pure metals after immersion in 3.5 wt% NaCl for 1 h.

parameter n is a measure of surface roughness, which has a value in the range of zero to unity and represents non-ideal capacitance loop [52]. The equivalent circuit (Fig. 3c) of electrodeposited Ni₉₀P₁₀, pure Ni, and MS 1008 contains elements corresponding to the solution resistance (R_s), pore capacitance (CPE_{pore}), pore resistance (R_{pore}), double-layer capacitance (CPE_{dl}), and charge transfer resistance (R_{ct}). The polarization resistance, $R_p = R_{ct} + R_{pore} - R_{ss}$, gives total resistance of the passive

film. The equivalent circuit (Fig. 3d) of electrodeposited $Ni_{85}P_{15}$, $Ni_{80}P_{20}$, $Co_{90}P_{10}$, $Co_{85}P_{15}$, $Co_{80}P_{20}$, and pure Co contains elements corresponding to the solution resistance (R_s), double-layer capacitance (CPE_{dl}), and charge transfer resistance (R_{ct}), where $R_{ct} - R_s$ gives the polarization resistance (R_p). The impedance data were well fitted by the proposed equivalent circuits using three criteria to evaluate the general fit and accuracy: visual fit to Nyquist and Bode plots, low standard errors

for every circuit element and low goodness of fit from Chi-Squared test [53]. The error associated with each element was lower than 5% and the goodness of fit was less than 10^{-4} , indicating accurate description of the studied systems. The equivalent circuit values obtained from EIS study are summarized in Table S1. Fig. 3e summarizes the polarization resistance of the EMGs, showing that the polarization resistance increases with increase in phosphorus content. An increase in R_p signifies an increase in corrosion resistance. The polarization resistance of pure Ni $(R_p^{Ni}=1.1~{\rm kohm\text{-}cm}^2)$ and pure Co $(R_p^{Co}=2.5~{\rm kohm\text{-}cm}^2)$ almost doubled with addition of 10 at% phosphorus, suggesting that the addition of phosphorus has a significant effect on the passive layer. The polarization resistance of the EMGs increased with increasing phosphorus content, for both the Ni-based and Co-based systems. Capacitance (C) of the passive film was extracted from the CPE element following Hsu and Mansfeld [54]:

$$C = Y_0(\omega_{max})^{n-1} \tag{4}$$

where, ω''_{max} is the characteristic frequency, C is the capacitance, Y_o is the frequency independent admittance of the CPE, and n is the exponent of the CPE. The characteristic frequency (ω''_{max}), is the frequency at which the imaginary part of the impedance (-Z'') is maximum [53], and is shown in Fig. 3(a & b). The exponent of the constant phase element (n_{dl}) represents deviation from pure capacitive behavior. Decrease in the value of n_{dl} (Fig. 3f) indicates a transition from capacitive behavior to more conductive behavior of the passive layer, possibly due to porosity and heterogeneities on the surface [55–57]. Increase in n_{dl} with increasing phosphorus content suggests that the passive layer got denser and pore-free with higher phosphorus content. The thickness (d) of the passive layer may be obtained from the capacitance (C) following Orazem [58,59]:

$$d = \varepsilon \varepsilon_0 / C$$
 (5)

where, ε is the dielectric constant and $\varepsilon_o = 8.8542 \times 10^{-14}$ F/cm is the permittivity of vacuum. According to Eq. 5, a decrease in dielectric constant and/or an increase in the capacitance of passive layer would indicate decrease in the thickness of the passive layer. The reciprocal of capacitance (1/C) of the surface film is directly proportional to its thickness. Fig. 3g shows the reciprocal of capacitance (1/C) values for the studied coatings, which increases with increase in phosphorus content, suggesting a similar trend for the passive film thickness. To deduce the film thickness, the dielectric constants for the passive films are needed, which in the case of Ni-P and Co-P systems are not known. The HRTEM image (Fig. S3) of Ni₈₀P₂₀ passive film at open circuit potential shows that the thickness of passive film ranges ~ 1 –9 nm. This would give a range in dielectric constant for the complex passive film on Ni₈₀P₂₀ coating using Eq. (5). Considering the complexity of the passive film and its non-ideal nature, the estimates for passive film thickness for other coatings may have a large margin of error since the dielectric constants of the complex passive films for Ni-P and Co-P system are not known. The impedance results for MS 1008 ($R_p^{MS} = 0.6 \text{ kohm-cm}^2$) showed that the passive layer was not protective, making it vulnerable to ion attack in NaCl electrolyte, highlighting the potential use of Ni-P and Co-P as protective coatings on steel components.

3.3. Potentiodynamic polarization

Potentiodynamic polarization studies for the Ni-based and Co-based alloys compared to mild steel (MS 1008) in 3.5 wt% sodium chloride (NaCl) solution were performed. A representative potentiodynamic polarization plot for $Ni_{80}P_{20}$ EMG is shown in Fig. 4. The corrosion potential (E_{corr}) and corrosion current density (j_{corr}) were calculated for all the alloys using Tafel extrapolation as shown in Fig. 4 for $Ni_{80}P_{20}$ EMG. The pitting potential (E_{pit}) and passivation range ($\Delta E = E_{pit} - E_{corr}$) were measured from the polarization curve as marked on the figure. The potentiodynamic polarization results for all the alloys are summarized in

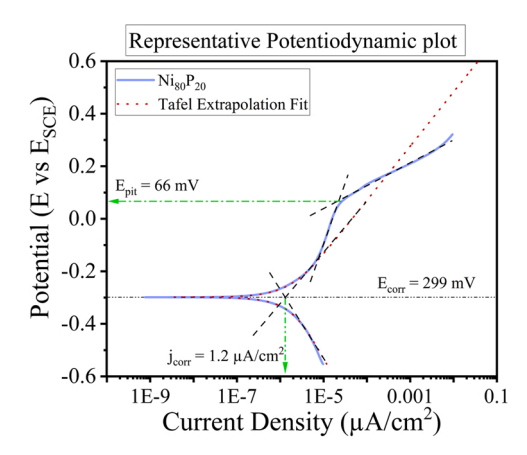


Fig. 4. A representative potentiodynamic polarization plot for $Ni_{80}P_{20}$ EMG for determining the corrosion potential (E_{corr}), corrosion current density (j_{corr}), and pitting potential (E_{pit}).

Table S2.

Fig. 5(a & b) summarize all the potentiodynamic polarization plots for the Ni-based and Co-based alloys compared to mild steel (MS 1008), respectively. The corrosion potential (E_{corr}) is primarily influenced by the chemistry of the electrical double layer (EDL) on the surface formed in equilibrium with the electrolyte [45]. Among the amorphous alloys, the corrosion potential (E_{corr}) increased towards nobler value with increase in phosphorus content for both the Ni-based and Co-based systems, as shown in Fig. 5c. The corrosion current density (j_{corr}) decreased by about an order of magnitude going from pure Ni $(13.6 \,\mu\text{A/cm}^2)$ to $Ni_{80}P_{20}$ EMG (1.2 μ A/cm²) and from pure Co (7.98 μ A/cm²) to $Co_{80}P_{20}$ EMG (0.854 μ A/cm²). Thus, the corrosion resistance improved significantly with the addition of phosphorus to pure nickel and pure cobalt. Among the amorphous alloys, the corrosion current density decreased with an increase in phosphorus content for both the Ni-based and Co-based systems, as shown in Fig. 5d. In addition, the anodic branch of the potentiodynamic plots shifted towards lower current densities with increase in phosphorus content (Fig. 5(a & b)). The alloys with 10 at% P (Ni₉₀P₁₀ and Co₉₀P₁₀) showed similar or higher corrosion current density compared to their corresponding pure metals, indicating that the addition of 10 at% P had a detrimental effect on corrosion resistance, possibly due to their inability to form a stable and compact passive film [32,33]. With increase in phosphorus content to 15 at%, the j_{corr} decreased and a distinct passive region was seen in the polarization plots for Ni₈₅P₁₅ and Co₈₅P₁₅. The Ni₈₀P₂₀ and Co₈₀P₂₀ alloys showed the lowest corrosion current densities in their respective systems, along with a significant increase in the passive region. The increase in passivation range with increasing phosphorus content may be attributed to the formation of a more protective surface layer. The surfaces for Ni₈₀P₂₀ and Co80P20 EMGs remained smooth and maintained their shiny appearance after the potentiodynamic polarization tests. In contrast, for Ni-P and Co-P EMGs with 10 at% P, the surface turned grayish after the polarization studies, as shown in the post-corrosion images in Fig. S4. All the electrodeposited alloys showed lower corrosion rate (v_{corr}) (Table S2) compared to mild steel (MS 1008). The trend of increase in corrosion resistance with increase in phosphorus content for both Niand Co-based systems from potentiodynamic polarization results agree with the impedance studies.

3.4. Surface analysis

3.4.1. X-ray photoelectron spectroscopy (XPS) analysis

The chemical nature of the passive layer was analyzed using XPS for $M_{90}P_{10}$ and $M_{80}P_{20}$ (M = Ni or Co) EMGs after polarization at different potentials. For $M_{80}P_{20}$ alloys, three polarization conditions were chosen as shown in Fig. 6, namely: (i) respective open-circuit potential (E_{OCP})

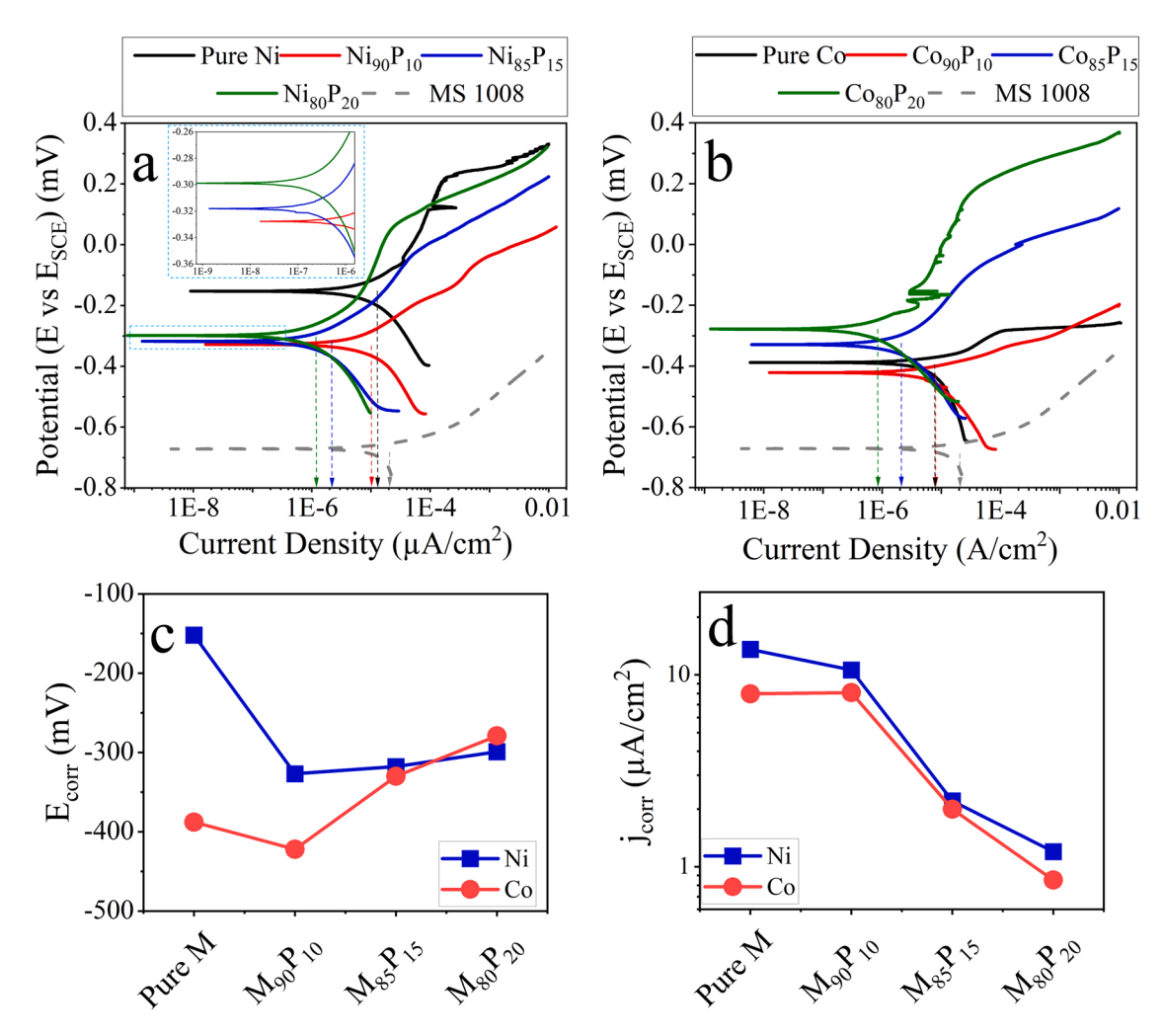


Fig. 5. Potentiodynamic polarization plots for (a) Ni-P and (b) Co-P alloys in comparison with the corresponding pure metals, and MS 1008 steel in 3.5 wt% NaCl at room temperature. The zoomed-in image shows the corrosion potential (E_{corr}) for Ni-P EMGs. The arrows show the corrosion current density of the respective sample; (c) corrosion potential (E_{corr}) and (d) corrosion current density (j_{corr}) versus composition of the Ni_{100-x}P_x and Co_{100-x}P_x EMGs (x = 10, 15, and 20 at%) and corresponding pure metals.

for 1 h, (ii) passive potential ($E_{OCP} + 200 \text{ mV}$) for 1 h, and (iii) transpassive potential (E_{OCP} + 600 mV) for 10 s. Two polarization conditions were chosen based on the potentiodynamic polarization plots of the M₉₀P₁₀ alloys as shown in Fig. S5, namely: (i) respective open-circuit potential (E_{OCP}) for 1 h, and (ii) trans-passive potential (E_{OCP} + 600 mV) for 10 s. The binding energies were calibrated based on the C 1 s peak value at 284.6 eV. The investigation was done within the binding energy spectrum of P_{2p} . The P_{2p} spectra were deconvoluted considering the binding energy of elemental phosphorus (P⁰ at 129.2 eV and 130.2 eV), hypophosphite anion (H₂PO₂) (P⁺ at 132.2 eV), and phosphate anion (H₂PO₄) (P⁵⁺ at 133.6 eV). According to the P-H₂O system Pourbaix diagram [60], the reaction of water with phosphorus, as shown by Eq. 6, results in the formation of a hypophosphite anion (H₂PO₂) layer on the alloy surface. The adsorbed hypophosphite anion oxidizes to phosphate anion at anodic potentials as illustrated by Eq. 7 and the rate of oxidation increases with increasing anodic overpotential.

$$P + 2H_2O \rightarrow H_2PO_2^- + 2H^+ + e^-$$
 (6)

$$H_2PO_2^2 + 2H_2O \rightarrow H_2PO_4^2 + 4H^+ + 3e^-$$
 (7)

The XPS spectra for $Ni_{80}P_{20}$ and $Co_{80}P_{20}$ at different potentials consisted of elemental P, hypophosphite anion, and phosphate anion peaks. The XPS spectra are shown in Fig. 6(a-c) for $Ni_{80}P_{20}$ and Fig. 6(d-f) for $Co_{80}P_{20}$ and the relative proportion of the peak intensities are

summarized in Fig. 6(g & h). The relative proportion of elemental P peak increased at the passive potential for both the EMGs and decreased at the trans-passive potential. The hypophosphite anion relative peak intensity became weaker, and the phosphate anion relative peak intensity became stronger with increasing anodic potential. This suggests that the EMG, when polarized to anodic potentials, underwent rapid oxidation of the hypophosphite anion into phosphate anion accompanied by dissolution of the phosphate species.

The XPS spectra for $Ni_{90}P_{10}$ consisted of elemental P and phosphate anion, as summarized in Fig. S5(a & b) An increase in polarization potential led to an increase in the concentration of phosphate anion and a decrease in the concentration of elemental P on the surface of the Ni₉₀P₁₀ EMG. Comparatively, different behavior was observed for $\text{Co}_{90}\text{P}_{10}$ EMG at similar surface polarization. The P_{2p} spectra consisted of an additional peak corresponding to hypophosphite anion, as shown in Fig. S5(c & d). The formation of the hypophosphite anion layer may be the significant contributing factor towards lower corrosion current density and higher polarization resistance of Co₉₀P₁₀ in contrast to Ni₉₀P₁₀ alloy. The role of hypophosphite anion layer may be to act as a barrier layer preventing dissolution by hydration of the surface. The EIS results for Co₉₀P₁₀ and Ni₉₀P₁₀ showed lower polarization resistance and n_{dl} values compared to high phosphorus containing EMGs, signifying that the passive layer in M₉₀P₁₀ alloys was porous, non-uniform, and less resistant to dissolution.

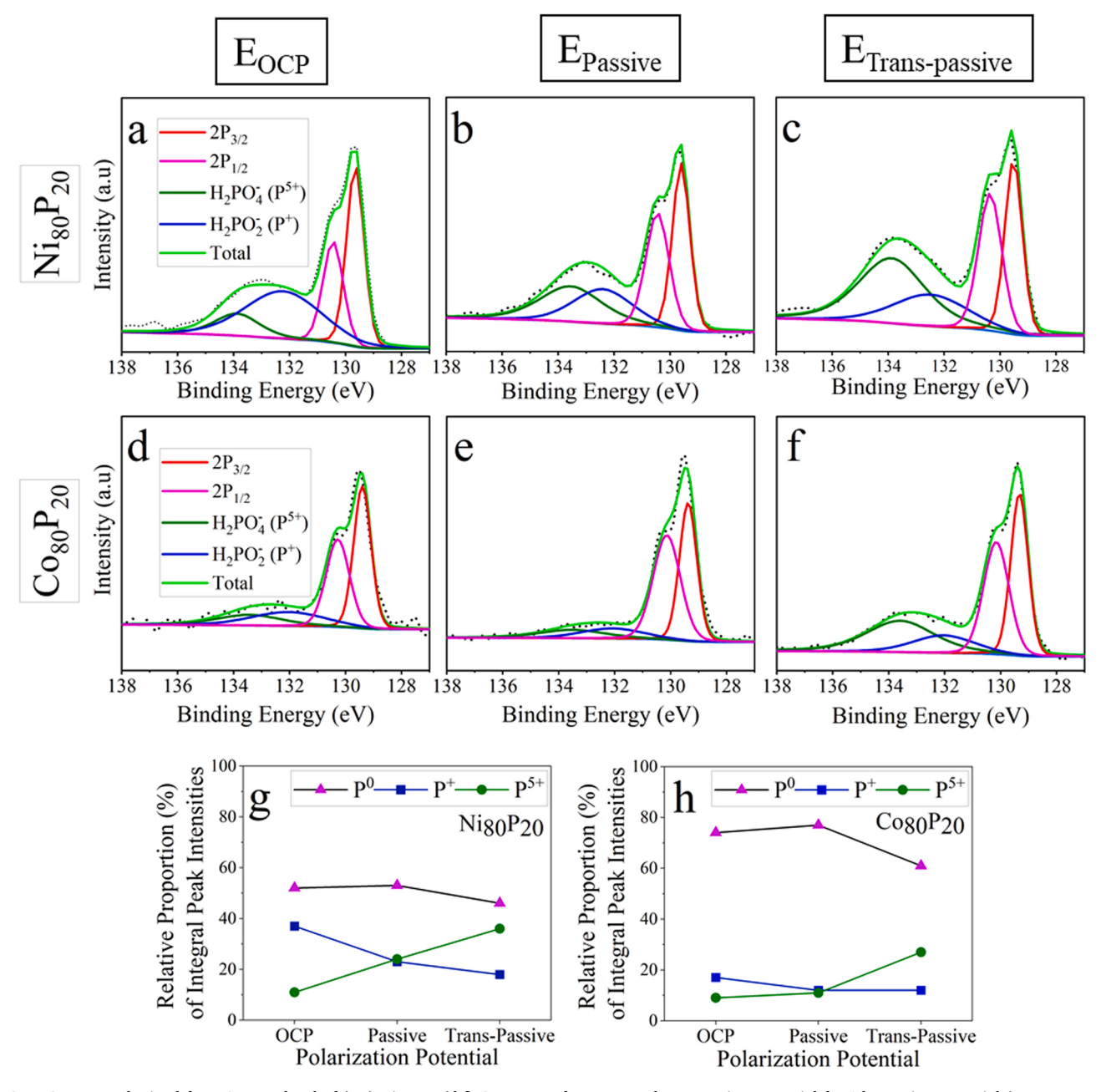


Fig. 6. XPS spectra obtained for P 2p core-level of (a-c) $Ni_{80}P_{20}$, (d-f) $Co_{80}P_{20}$ surfaces exposed to corrosion potential for 1 h, passive potential ($E_{Passive} = E_{OCP} + 200 \text{ mV}$) for 1 h, and trans-passive potential ($E_{Trans-passive} = E_{OCP} + 600 \text{ mV}$) for 10 s in 3.5 wt% NaCl solution. The relative peak intensities of elemental P, hypophosphite, and phosphate for (g) $Ni_{80}P_{20}$ and (h) $Co_{80}P_{20}$ are summarized.

3.4.2. Transmission Electron Microscopy (TEM) and Atom Probe Topography (APT) analysis

The XPS spectra for both $Ni_{80}P_{20}$ and $Co_{80}P_{20}$ consisted of hypophosphite, phosphate, and elemental P peaks with similar changes in relative peak intensity, suggesting a similar corrosion mechanism for both the binary alloys. $Ni_{80}P_{20}$ was selected as a representative alloy for further structural characterization using TEM and APT. Fig. S6a shows the Nyquist plots at different immersion times up to 5 days in 3.5 wt% NaCl for $Ni_{80}P_{20}$ EMG. The variation in polarization resistance with time is summarized in Fig. S6b. The polarization resistance for $Ni_{80}P_{20}$ didn't change much within the first 10 h of immersion (R_p after 1 h = 26.7 kohm-cm² and R_p after 10 h = 27.06 kohm-cm²). To ensure that the airformed film was replaced by a passive layer formed when exposed to 3.5 wt% NaCl solution, the TEM, and APT characterization were done for $Ni_{80}P_{20}$ EMG after 10 h at the open-circuit potential. Fig. 7a shows a

high-resolution TEM (HRTEM) image of the cross-section of the Pt protective layer/Ni-Cr coating/passive layer/base alloy. Fig. 7b shows the HRTEM image of the passive layer/base alloy interface that is marked by the white box in Fig. 7a. The SAD pattern shows diffused rings implying that the passive layer was amorphous. The amorphous structure of the passive layer offers improved corrosion resistance due to the lack of grain boundaries, which may decrease ion migration rates and make the passive layer more protective. Fig. 7c shows the SEM image of the APT needle with a white line illustrating the region where the data was reconstructed. The 3D APT reconstructed elemental map of the Cr coating/passive layer/base alloy is presented in Fig. 7d, while Fig. 7e has the one-dimensional composition profiles estimated using a cylindrical (diameter = 15 nm, length = 25 nm) region of interest that spans from the Cr coating through the passive layer into the base alloy. The composition profile obtained here shows that the passive layer is

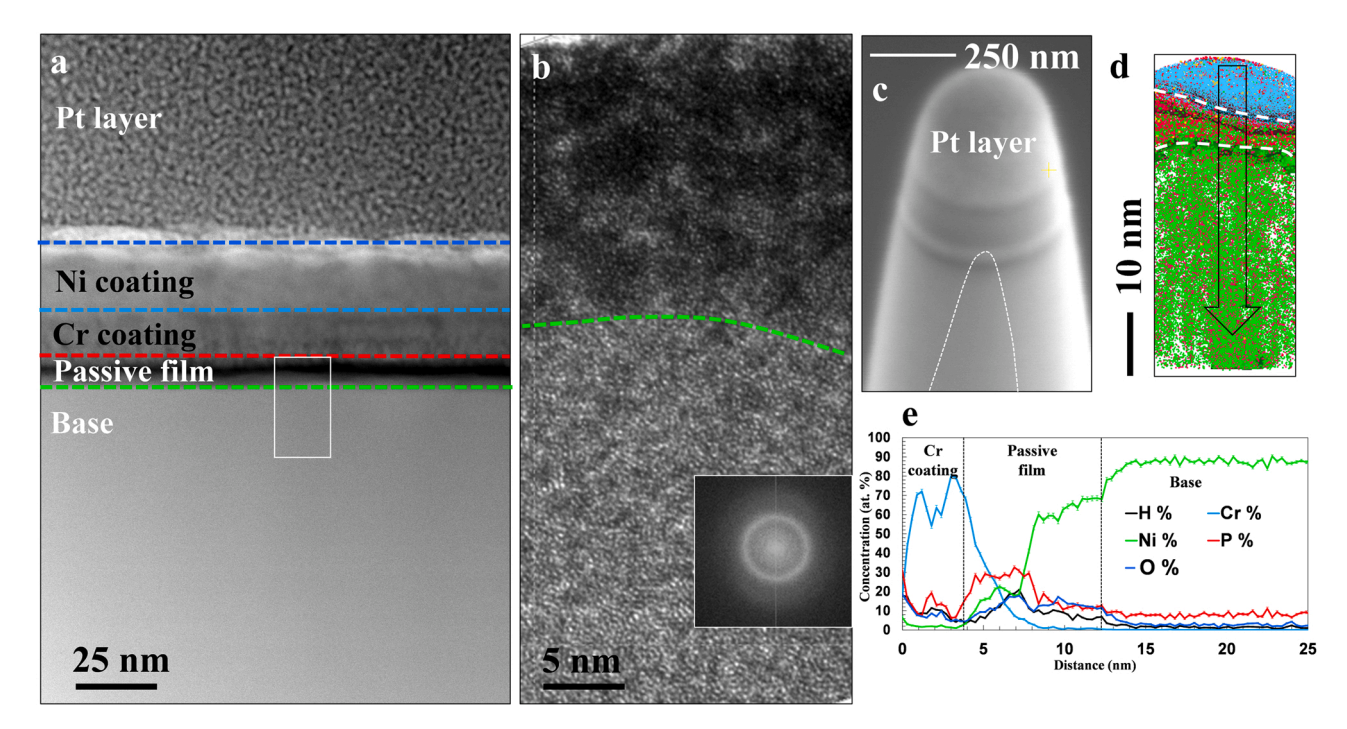


Fig. 7. Structure and composition across the passive film/ $Ni_{80}P_{20}$ base alloy after immersion in 3.5 wt% NaCl for 10 h at E_{corr} , then sputter-coated with Cr and Ni: (a) low-magnification HAADF STEM image of the Pt protective layer/Ni-Cr coating/passive film/ $Ni_{80}P_{20(Base)}$; (b) high magnification HRTEM image of the passive film/substrate interface highlighted by the white rectangle in (a) with SADP showing diffused rings indicating amorphous structure as an inset; (c) SEM image of the APT needle apex obtained by annular milling, with a white line denoting the region from which data was reconstructed; (d) 3D element distribution map of the Cr coating/passive film/base alloy, with an arrow indicating region where a concentration profile (shown in (e)) was calculated using a cylinder region of interest with diameter 15 nm and length of 25 nm; (e) Concentration profile, with 0.2 nm bin width, from Cr coating through the passive layer and into the base alloy.

rich in phosphorus. The underestimation of phosphorus in the base alloy may be attributed to the formation of neutral species of the metalloids that are not accelerated by the potential difference in the atom probe and go undetected [61–63]. XPS spectra for $M_{80}P_{20}$ EMGs (M = Ni or Co) showed that the majority of the phosphorus remained in the elemental form on the surface rather than forming hypophosphite or phosphate. The APT compositional (at%) data suggests that there is an enrichment of phosphorus at the passive layer/base material interface. Similar enrichment of phosphorus under the passive film was observed in Fe $_{70}Cr_{10}P_{13}C_7$ BMG in acidic electrolytes [64,65].

The Ni₉₀P₁₀ and Co₉₀P₁₀ alloys showed similar corrosion resistance compared to pure Ni and pure Co, which may be attributed to the lower phosphorus content in these EMGs that is insufficient to form a uniform and pore-free hypophosphite layer. Thus, no passive region (Fig. 5(a & b)) was observed in $M_{90}P_{10}$ EMGs (M = Ni or Co) and the alloy surface was active at anodic potentials. The EIS data (Fig. 3(e-g)) for M₉₀P₁₀ EMGs showed lower R_p , lower 1/C, and lower passive film thickness (d) compared to both $M_{85}P_{15}$ and $M_{80}P_{20}$, indicating the inferior characteristics of the passive layer in the alloys with 10 at% P. Increase in phosphorus content to 15 at% resulted in a significant improvement in corrosion resistance for both the alloy systems. The M₈₅P₁₅ alloys showed a sharp decrease in corrosion current density as well as good passivation (Table S2), while the polarization resistance increased by an order of magnitude (Fig. 3e). These results suggest that the amount of phosphorus in $M_{85}P_{15}$ was sufficient to form a protective hypophosphite layer, with further improvement seen for $\mathrm{M}_{80}\mathrm{P}_{20}$ alloys. Comparing the two systems, the Co-based alloys showed better corrosion resistance than the corresponding Ni-based alloys, which may be due to the difference in the pure metal dissolution rates. From the potentiodynamic polarization results, pure Ni $(j_{corr}^{Ni} = 17.6 \,\mu\text{A/cm}^2)$ showed more than twice the corrosion current density compared to pure Co (j_{corr}^{Co} = $7.09 \, \mu A/cm^2$).

From the combined XPS and TEM/APT analysis, the passivation mechanism in the EMG coatings seem to be controlled by the

hypophosphite anion layer along with the phosphorus enriched layer, as illustrated schematically in Fig. 8. When the metallic glass is exposed to 3.5 wt% NaCl solution under open-circuit condition, metal dissolution occurs preferentially. Due to the slow oxidation of phosphorus, there is enrichment of phosphorus on the surface, followed by the formation of hypophosphite layer above the phosphorus enriched layer. Metal dissolution continues until the formation of a compact hypophosphite film which blocks the electrolyte from reaching the base alloy, as schematically shown in Fig. 8a. The XPS data showed decrease in the relative proportion of hypophosphite and increase in phosphate at

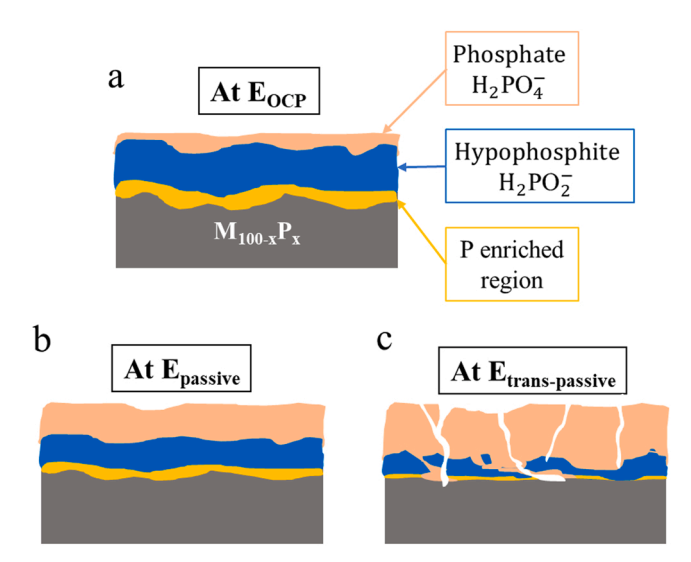


Fig. 8. A schematic representation of the corrosion mechanism of $M_{100-x}P_{x\geq 15}$ (M=Ni or Co) alloy with increasing anodic potential; (a) at open circuit potential (E_{OCP}); (b) in the passive region ($E_{passive}$); (c) in the trans-passive region ($E_{trans-passive}$).

potentials in the passive region, as shown schematically in Fig. 8b. XPS analysis for $Ni_{80}P_{20}$ and $Co_{80}P_{20}$ (Fig. 6) indicates that the phosphate layer is non-passivating since its relative peak intensity increased with the increase in anodic potential. Polarization to anodic potentials promotes the oxidation of hypophosphite layer to phosphate anions, which dissolves in the electrolyte providing the electrolyte access to the enriched phosphorus layer. The hypophosphite layer is formed again by the reaction of water with the phosphorus-rich layer, thereby repassivating the surface and controlling the dissolution rate of metal atoms through it via diffusion. Trans-passive dissolution commences once the oxidation rate of the hypophosphite layer is faster than its formation rate and there is consequent breakdown of the passive film as shown schematically in Fig. 8c.

3.4.3. Scanning Kelvin Probe (SKP)

Scanning Kelvin Probe (SKP) was used for measuring the relative SKP potential with respect to tungsten probe and correlating electronic structure to the corrosion resistance of the amorphous alloys. SKP potential has been correlated with electron work function (EWF) to explain the corrosion behavior in earlier studies [48,66]. A nobler surface is associated with a higher work function, which is directly related to the ease of electron removal [67]. SKP potential measured in air for several metals was found to vary linearly with their corrosion potential in aqueous solution [68]. An inverse correlation between the measured SKP potential difference and the corrosion behavior was also observed [69]. Although there are several reports on the correlations between SKP potential and corrosion behavior in different electrolytes, these may not be universally valid and needs to be evaluated for each new system independently [70,71]. The relative SKP potential (or relative electron work function) increased by around 40% for the Ni_{100-x}P_x system and around 60% for the $Co_{100-x}P_x$ system with increase in phosphorus content (x) from 10 at%P to 20 at%P, as shown in Fig. 9(a & b). Correspondingly, the corrosion current density (j_{corr}) measured from potentiodynamic polarization decreased with increase in phosphorus content from 10-20 at%P. This suggests an inverse correlation between the relative work function and corrosion current density among the EMGs. The binding energy of P_{2p} measured using XPS explains the trend in relative electron work function with increasing phosphorus for both the Ni-P and Co-P systems. A slight shift in P⁰ peak position was observed for the Ni-P and Co-P metallic glasses compared to pure elemental P (red or black phosphorus). Depending on the quantity of metal (Ni or Co) and their electronegativity, P becomes negatively charged because of partial covalent bonding between Ni_{3d} (or Co_{2p}) and P_{2p} [72–74]. This shifts the Ni_{3d} (or Co 2p) bands away from the Fermi level (E_F) to higher binding energies while it reduces the P_{2p} binding energy. The P_{2p} binding energy was slightly lower for Ni₈₀P₂₀ (129.4 eV) and $Co_{80}P_{20}$ (129.4 eV) compared to $Ni_{90}P_{10}$ (129.6 eV) and $Co_{90}P_{10}$ (129.7 eV). The lower binding energy of P_{2p} in the metallic glasses with

higher phosphorus content may be attributed to the higher density of shared electrons and stronger covalent bonds in these alloys. The stronger (Co, Ni)-P bond increases the electron work function and makes charge transfer to adsorbed species more difficult. In sum, for both the Ni-P and Co-P systems, higher relative work function for the metallic glasses with larger fraction of phosphorus contributed towards their greater corrosion resistance and chemical stability.

4. Conclusion

The corrosion behavior and passive film characteristics of model binary Co-P and Ni-P amorphous alloys were investigated using accelerated corrosion tests along with their electron work function using Scanning Kelvin Probe. The main conclusions are summarized below:

- The higher phosphorus containing alloys showed better corrosion resistance in both the systems. The corrosion current density of $M_{80}P_{20}$ alloys (Ni $_{80}P_{20}\sim1.2~\mu\text{A/cm}^2$ and $Co_{80}P_{20}\sim0.854~\mu\text{A/cm}^2)$ was lower by an order of magnitude compared to M₉₀P₁₀ alloys $(Ni_{90}P_{10} \sim 10.6 \,\mu\text{A/cm}^2 \text{ and } Co_{90}P_{10} \sim 8.09 \,\mu\text{A/cm}^2)$. The $M_{80}P_{20}$ alloys also showed a large passivation region ($Ni_{80}P_{20} \sim 365$ mV and $Co_{80}P_{20} \sim 470 \text{ mV}$) while the $M_{90}P_{10}$ alloys did not show any passivation. The corrosion potential increased towards nobler values with increasing phosphorus content, Ni-based EMGs showed an increase of 28 mV ($Ni_{90}P_{10} = -327$ mV to $Ni_{80}P_{20} = -299$ mV), and Co-based EMGs showed an increase of 143 mV ($Co_{90}P_{10} = -422$ mV to $Co_{80}P_{20} = -279$ mV). Between the two alloy systems, the Cobased EMGs showed lower corrosion current, larger passivation region, and higher polarization resistance, suggesting that the Cobased alloys are more corrosion resistant compared to the corresponding Ni-based alloys.
- EIS results showed that the $M_{80}P_{20}$ EMGs had an order of magnitude higher polarization resistance ($Ni_{80}P_{20} \sim 26.07 \text{ kohm-cm}^2$ and $Co_{80}P_{20} \sim 58 \text{ kohm-cm}^2$) compared to $M_{90}P_{10}$ EMGs ($Ni_{90}P_{10} \sim 2.5 \text{ kohm-cm}^2$ and $Co_{90}P_{10} \sim 5.55 \text{ kohm-cm}^2$). The $M_{80}P_{20}$ EMGs showed recipocal of capacitance values higher by an order of magnitude and exponent of constant phase element (n_{dl}) values close to unity, indicating more capacitive nature of the passive film than for the alloys with the lower phosphorus content.
- XPS spectra for Ni₈₀P₂₀ and Co₈₀P₂₀ EMGs at different potentials indicated the presence of elemental P, hypophosphite, and phosphate layers on the surface. The hypophosphite peak intensity became relatively weaker, and the phosphate peak intensity became relatively stronger with increasing anodic potentials.
- TEM/APT complementary studies were done for structural characterization of the passive film formed for Ni₈₀P₂₀. The SAD pattern indicated that the passive layer was amorphous. APT composition profile showed enrichment of phosphorus at the passive layer/base

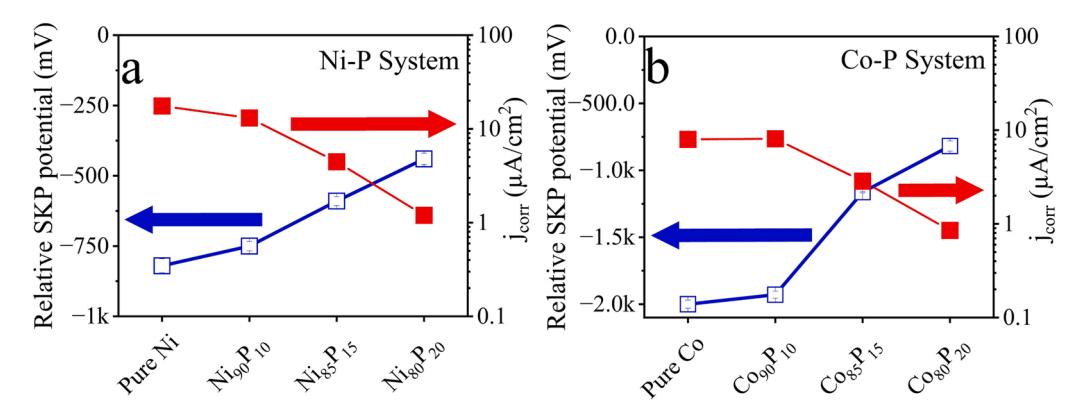


Fig. 9. Relative SKP potential (primary y-axis) and corrosion current density (secondary y-axis) as a function of composition for (a) Ni-P and (b) Co-P EMGs and the corresponding pure metals. The error in SKP potential values is estimated to be \pm 3%.

alloy interface and the passivation mechanism dictated by the impervious and compact hypophosphite layer.

• The relative SKP potential (or relative electron work function) increased by ~ 40% for the Ni-P system and ~ 60% for the Co-P system with increase in phosphorus content from 10 at%P to 20 at %P. The lower binding energy of P 2p in the metallic glasses with higher P content was attributed to the higher density of shared electrons in the partial covalent bonds in these alloys. The higher electron work function for the metallic glasses with larger fraction of phosphorus likely contributed towards their greater corrosion resistance and chemical stability.

CRediT authorship contribution statement

Chaitanya Mahajan: Conceptualization, Data curation, Formal analysis, Methodology, Writing — original draft. Vahid Hasannaeimi: Methodology, Formal analysis, Writing — review & editing. Mayur Pole: Methodology, Formal analysis, Writing — review & editing. Elizabeth Kautz: Methodology, Formal analysis, Writing — review & editing. Bharat Gwalani: Methodology, Formal analysis, Writing — review & editing. Sundeep Mukherjee: Conceptualization, Project administration, Resources, Supervision, Writing — review & editing.

Declaration of Competing Interest

The authors declare that they have no known competing financial interests or personal relationships that could have appeared to influence the work reported in this paper.

Data availability

Data will be made available on request.

Acknowledgments

This work was partly supported by funding from the National Science Foundation (NSF), U.S.A., under grant numbers 1561886, 1919220, and 1762545. Any opinions, findings, and conclusions expressed in this paper are those of the authors and do not necessarily reflect the views of NSF. B.G. would like to acknowledge Pacific Northwest National Laboratory's (PNNL's) Directed Research and Development Program - Solid Phase Processing Science Initiative. PNNL is a multiprogram national laboratory operated for the Department of Energy (DOE), U.S.A., by Battelle Memorial Institute under Contract No. DE-AC05–76RL0–1830.

Data Availability

The data supporting the findings of this study are available within the article and its supplementary materials.

Appendix A. Supporting information

Supplementary data associated with this article can be found in the online version at doi:10.1016/j.corsci.2022.110578.

References

- [1] W.K. Jun, R.H. Willens, P. Duwez, Non-crystalline structure in solidified gold-silicon alloys, Nature 187 (1960) 869–870, https://doi.org/10.1038/ 187869h0
- [2] H. Choi-Yim, W.L. Johnson, Bulk metallic glass matrix composites, Appl. Phys. Lett. 71 (1997) 3808–3810. https://doi.org/10.1063/1.120512.
- [3] W.L. Johnson, Bulk glass-forming metallic alloys: science and technology, MRS Bull. 24 (1999) 42–56, https://doi.org/10.1557/S0883769400053252.
- [4] W.H. Wang, C. Dong, C.H. Shek, Bulk metallic glasses, Mater. Sci. Eng. R: Rep. 44 (2004) 45–89, https://doi.org/10.1016/j.mser.2004.03.001.
- [5] M.F. Ashby, A.L. Greer, Metallic glasses as structural materials, Scr. Mater. 54 (2006) 321–326, https://doi.org/10.1016/j.scriptamat.2005.09.051.

- [6] C. Suryanarayana, A. Inoue, Bulk Metallic Glasses, 2nd Editio, CRC Press, 2017, https://doi.org/10.1201/9781315153483.
- [7] J.J. Kruzic, Bulk metallic glasses as structural materials: a review, Adv. Eng. Mater. 18 (2016) 1308–1331, https://doi.org/10.1002/adem.201600066.
- [8] A. Aditya, H. Felix Wu, H. Arora, S. Mukherjee, Amorphous metallic alloys: pathways for enhanced wear and corrosion resistance, JOM 69 (2017) 2150–2155, https://doi.org/10.1007/s11837-017-2384-9.
- [9] H.S. Arora, H.S. Grewal, H. Singh, S. Mukherjee, Zirconium based bulk metallic glass—Better resistance to slurry erosion compared to hydroturbine steel, Wear 307 (2013) 28–34, https://doi.org/10.1016/J.WEAR.2013.08.016.
- [10] A. Inoue, Stabilization of metallic supercooled liquid and bulk amorphous alloys, Acta Mater. 48 (2000) 279–306, https://doi.org/10.1016/S1359-6454(99)00300-
- [11] M. Telford, The case for bulk metallic glass, Mater. Today 7 (2004) 36–43, https://doi.org/10.1016/S1369-7021(04)00124-5.
- [12] J. Schroers, Q. Pham, A. Desai, Thermoplastic forming of bulk netallic glass A technology for MEMS and microstructure fabrication, J. Micro Syst. 16 (2007) 240–247, https://doi.org/10.1109/JMEMS.0007.892889.
- [13] J. Schroers, Processing of bulk metallic glass, Adv. Mater. 22 (2010) 1566–1597, https://doi.org/10.1002/adma.200902776.
- [14] D.C. Hofmann, J.Y. Suh, A. Wiest, G. Duan, M.L. Lind, M.D. Demetriou, W. L. Johnson, Designing metallic glass matrix composites with high toughness and tensile ductility, Nature 451 (2008) 1085–1089, https://doi.org/10.1038/nature06598.
- [15] V. Hasannaeimi, S. Muskeri, B. Gwalani, D.C. Hofmann, S. Mukherjee, Deformation behavior of metallic glass composites and plasticity accommodation at microstructural length-scales, Mater. Today Commun. 24 (2020), 101237, https:// doi.org/10.1016/J.MTCOMM.2020.101237.
- [16] S.S Joshi, S Katakam, H.S. Arora, S Mukhejree, N.B. Dahotre, Amorphous Coatings and Surfaces on Structural Materials, Critical Reviews in Solid State and Materials Sciences 41 (1) (2016) 1–46, https://doi.org/10.1080/10408436.2015.1053602.
- [17] Q. Luo, Y.J. Sun, J. Jiao, Y.X. Wu, S.J. Qu, J. Shen, Formation and tribological behavior of AC-HVAF-sprayed nonferromagnetic Fe-based amorphous coatings, Surf. Coat. Technol. 334 (2018) 253–260, https://doi.org/10.1016/j. surfcoat.2017.11.042.
- [18] C.M. Lee, J.P. Chu, W.Z. Chang, J.W. Lee, J.S.C. Jang, P.K. Liaw, Fatigue property improvements of Ti-6Al-4V by thin film coatings of metallic glass and TiN: A comparison study, Thin Solid Films 561 (2014) 33–37, https://doi.org/10.1016/j. tsf.2013.08.027.
- [19] J.B. Cheng, X.B. Liang, B.S. Xu, Devitrification of arc-sprayed FeBSiNb amorphous coatings: Effects on wear resistance and mechanical behavior, Surf. Coat. Technol. 235 (2013) 720–726. https://doi.org/10.1016/j.surfcoat.2013.08.054.
- [20] S.S. Joshi, J.Z. Lu, N.B. Dahotre, Optimization of laser thermal treatment of Fe–Si–B metallic glass, J. Manuf. Process. 24 (2016) 31–37, https://doi.org/ 10.1016/j.jmapro.2016.07.004.
- [21] V. Hasannaeimi, X. Wang, R. Salloom, Z. Xia, J. Schroers, S. Mukherjee, Nanomanufacturing of Non-Noble Amorphous Alloys for Electrocatalysis, ACS Appl. Energy Mater. 3 (2020) 12099–12107, https://doi.org/10.1021/ acsaem.0c02221.
- [22] M. Sadeghilaridjani, Y. Chia Yang, V. Hasannaeimi, C. Mahajan, S. Jha, M. Pole, Z. Xia, S. Mukherjee, Multiscale manufacturing of amorphous alloys by a facile electrodeposition approach and their property dependence on the local atomic order, ACS Appl. Mater. amp; Interfaces 0 (2021), https://doi.org/10.1021/acsami.0c22153.
- [23] V. Hasannaeimi, S. Mukherjee, Highly catalytic amorphous Ni–P synthesized via pulsed electrodeposition, Adv. Eng. Mater. 21 (2019) 1–7, https://doi.org/ 10.1002/adem.201801122.
- [24] M. Sadeghilaridjani, A. Ayyagari, S. Muskeri, V. Hasannaeimi, J. Jiang, S. Mukherjee, Small-Scale Mechanical Behavior of Ion-Irradiated Bulk Metallic Glass, JOM 2019 72:1 72 (2019) 123–129, https://doi.org/10.1007/S11837-019-03848-3.
- [25] V. Hasannaeimi, M. Sadeghilaridjani, S. Mukherjee. Electrochemical and Corrosion Behavior of Metallic Glasses, MDPI Books, Basel, Switzerland, 2021.
- [26] H. Chiriac, A.E. Moga, M. Urse, I. Paduraru, N. Lupu, Preparation and magnetic properties of amorphous NiP and CoP nanowire arrays, J. Magn. Magn. Mater. 272–276 (2004) 1678–1680, https://doi.org/10.1016/J.JMMM.2003.12.540.
- [27] M. Fernández, J.M. Martínez-Duart, J.M. Albella, Electrical properties of electroless Ni-P thin films, Electrochim. Acta 31 (1986) 55–57, https://doi.org/ 10.1016/0013-4686(86)80060-3.
- [28] G. Salvago, G. Fumagalli, Electroless nickel:defects, passivity and localized corrosion, Met. Finish. 85 (3) (1987) 31–35.
- [29] M. Pole, M. Sadeghilaridjani, J. Shittu, C. Mahajan, N. Ghodki, S. Mukherjee, Electrodeposited metallic glasses with superlative wear resistance, Mater. Sci. Eng.: A 816 (2021), 141315, https://doi.org/10.1016/j.msea.2021.141315.
- [30] S.B. Antonelli, T.L. Allen, D.C. Johnson, V.M. Dubin, Determining the Role of W in Suppressing Crystallization of Electroless Ni–W–P Films, J. Electrochem. Soc. 153 (2006) J46, https://doi.org/10.1149/1.2193332.
- [31] P.G. Kotula, S.V. Prasad, Visualization of Kirkendall Voids at Cu-Au Interfaces by In Situ TEM Heating Studies, Jom 71 (2019) 3521–3530, https://doi.org/10.1007/ s11837-019-03708-0.
- [32] J. Flis, D.J. Duquette, Effect of phosphorus on anodic dissolution and passivation of nickel in near-neutral solutions, Corrosion 41 (1985) 700–706, https://doi.org/ 10.5006/1.3583006.
- [33] R.B. Diegle, N.R. Sorensen, C.R. Clayton, M.A. Helfand, Y.C. Yu, An XPS Investigation into the Passivity of an Amorphous Ni-20P Alloy, J. Electrochem. Soc. 135 (2019) 1085–1092, https://doi.org/10.1149/1.2095880.

- [34] H. Habazaki, S.Q. Ding, A. Kawashima, K. Asami, K. Hashimoto, A. Inoue, T. Masumoto, The anodic behavior of amorphous Ni-19P alloys in different amorphous states, Corros. Sci. 29 (1989) 1319–1328, https://doi.org/10.1016/ 0010-938X(89)90122-4.
- [35] N.R. Sorensen, F.J. Hunkeler, R.M. Latanision, The Anodic Polarization Behavior of Fe-Ni-P-B and Fe-Ni-Cr-P-B Amorphous Alloys, Corrosion 40 (1984) 619–624, https://doi.org/10.5006/1.3581928.
- [36] Ratzker, Menahem, David S. Lashmore, and John A. Tesk. "Electroforming of metallic glasses for dental applications." U.S. Patent 5,316,650, issued May 31, 1994.
- [37] M. Saitou, Y. Okudaira, W. Oshikawa, Amorphous structures and kinetics of phosphorous incorporation in electrodeposited Ni-P thin films, J. Electrochem. Soc. 150 (2003) C140, https://doi.org/10.1149/1.1545459.
- [38] Eds. Schlesinger, Mordechay, and Milan Paunovic, Modern Electroplating: Fifth Edition, Vol. 55 (2010) 2011, doi: 10.1002/9780470602638.
- [39] N. Ibl, Some theoretical aspects of pulse electrolysis, Surf. Technol. 10 (1980) 81–104, https://doi.org/10.1016/0376-4583(80)90056-4.
- [40] J. Ren, C. Mahajan, L. Liu, D. Follette, W. Chen, S. Mukherjee, Corrosion behavior of selectively laser melted CoCrFeMnNi high entropy alloy, Met. (Basel) 9 (2019), https://doi.org/10.3390/met9101029.
- [41] A.Y. Gerard, J. Han, S.J. McDonnell, K. Ogle, E.J. Kautz, D.K. Schreiber, P. Lu, J. E. Saal, G.S. Frankel, J.R. Scully, Aqueous passivation of multi-principal element alloy Ni38Fe20Cr22Mn10Co10: Unexpected high Cr enrichment within the passive film, Acta Mater. 198 (2020) 121–133, https://doi.org/10.1016/j.actamat 2020 07 024
- [42] B.P. Daly, F.J. Barry, Electrochemical nickel-phosphorus alloy formation, Int. Mater. Rev. 48 (2003) 326–338, https://doi.org/10.1179/095066003225008482
- [43] X. Li, L. Wang, L. Fan, Z. Cui, M. Sun, Effect of temperature and dissolved oxygen on the passivation behavior of Ti–6Al–3Nb–2Zr–1Mo alloy in artificial seawater, J. Mater. Res. Technol. 17 (2022) 374–391, https://doi.org/10.1016/J. JMRT.2022.01.018.
- [44] Z. Wang, Z. Feng, L. Zhang, Effect of high temperature on the corrosion behavior and passive film composition of 316 L stainless steel in high H2S-containing environments, Corros. Sci. 174 (2020), 108844, https://doi.org/10.1016/J. CORSCI.2020.108844.
- [45] D.J. Mills, An introduction to electrochemical corrosion testing for practicing engineers and scientists, Prog. Org. Coat. 26 (1995) 73–74, https://doi.org/ 10.1016/0300-9440(95)90005-5.
- [46] H. Ashassi-Sorkhabi, M. Es'haghi, Corrosion resistance enhancement of electroless Ni-P coating by incorporation of ultrasonically dispersed diamond nanoparticles, Corros. Sci. 77 (2013) 185–193, https://doi.org/10.1016/j.corsci.2013.07.046.
- [47] Y. Zou, Z. Zhang, S. Liu, D. Chen, G. Wang, Y. Wang, M. Zhang, Y. Chen, Ultrasonic-Assisted Electroless Ni-P Plating on Dual Phase Mg-Li Alloy, J. Electrochem. Soc. 162 (2015) C64–C70, https://doi.org/10.1149/2.0841501jes.
- [48] V. Hasannaeimi, A.V. Ayyagari, S. Muskeri, R. Salloom, S. Mukherjee, Surface degradation mechanisms in a eutectic high entropy alloy at microstructural lengthscales and correlation with phase-specific work function, Npj Mater. Degrad. 3 (2019) 1–8, https://doi.org/10.1038/s41529-019-0079-0.
- [49] A. Fattah-Alhosseini, S. Vafaeian, Influence of grain refinement on the electrochemical behavior of AISI 430 ferritic stainless steel in an alkaline solution, Appl. Surf. Sci. 360 (2016) 921–928, https://doi.org/10.1016/j.
- [50] G.J. Brug, A.L.G. Van Den Eeden, M. Sluyters-rehbach, J.H. Sluyters, T.H. E. ANALYSIS, The analysis of electrode impedances complicated by the presence of a constant phase element, J. Electro Chem. 176 (1984) 275–295, https://doi.org/ 10.1016/S0022-0728(84)80324-1.
- [51] J.B. Jorcin, M.E. Orazem, N. Pébère, B. Tribollet, CPE analysis by local electrochemical impedance spectroscopy, Electrochim. Acta 51 (2006) 1473–1479, https://doi.org/10.1016/J.ELECTACTA.2005.02.128.
- [52] H. Ashassi-Sorkhabi, M. Es'haghi, Corrosion resistance enhancement of electroless Ni–P coating by incorporation of ultrasonically dispersed diamond nanoparticles, Corros. Sci. 77 (2013) 185–193, https://doi.org/10.1016/j.corsci.2013.07.046.
- [53] M.E. Orazem, B. Tribollet, Electrochemical Impedance Spectroscopy, Electrochemical Impedance, Spectroscopy (2008) 1–523, https://doi.org/10.1002/ 9780470381588.
- [54] C. Hsu, F.M.- Corrosion, Concerning the conversion of the constant phase element parameter Y0 into a capacitance, Corrosion 57 (9) (2001) 747–748, doi:10.5006/ 1.3280607.
- [55] E.M. Fayyad, A.M. Abdullah, M.K. Hassan, A.M. Mohamed, C. Wang, G. Jarjoura, Z. Farhat, Synthesis, characterization, and application of novel Ni-P-carbon nitride

- nanocomposites, Coatings 8 (2018) 1–13, https://doi.org/10.3390/
- [56] A. Stankiewicz, J. Masalski, B. Szczygieł, Impedance spectroscopy studies of electroless Ni-P matrix, Ni-W-P, Ni-P-ZrO2, and Ni-W-P-ZrO2 coatings exposed to 3.5% NaCl solution, Mater. Corros. 64 (2013) 908–913, https://doi.org/10.1002/ macc. 201206856
- [57] P.L. Cabot, J.A. Garrido, E. Pe'rez, A.H. Moreira, P.T.A. Sumodjo, W. Proud, Eis study of heat-treated Al-Zn-Mg alloys in the passive and transpassive potential regions, Electrochim. Acta 40 (1995) 447–454, https://doi.org/10.1016/0013-4686(94)00299-G.
- [58] M.E. Orazem, I. Frateur, B. Tribollet, V. Vivier, S. Marcelin, N. Pébère, A.L. Bunge, E.A. White, D.P. Riemer, M. Musiani, Dielectric Properties of Materials Showing Constant-Phase-Element (CPE) Impedance Response, J. Electrochem. Soc. 160 (2013) C215–C225, https://doi.org/10.1149/2.033306jes.
- [59] B. Hirschorn, M.E. Orazem, B. Tribollet, V. Vivier, I. Frateur, M. Musiani, Determination of effective capacitance and film thickness from constant-phaseelement parameters, Electrochim. Acta 55 (2010) 6218–6227, https://doi.org/ 10.1016/J.ELECTACTA.2009.10.065.
- [60] M. Pourbaix, H. Zhang, A. Pourbaix, Presentation of an Atlas of chemical and electrochemical equilibria in the presence of a gaseous phase, Mater. Sci. Forum 251–254 (1997) 143–148, https://doi.org/10.4028/www.scientific.net/msf.251-254 143
- [61] A. Devaraj, R. Colby, W.P. Hess, D.E. Perea, S. Thevuthasan, Role of Photoexcitation and Field Ionization in the Measurement of Accurate Oxide Stoichiometry by Laser-Assisted Atom Probe Tomography, J. Phys. Chem. Lett. 4 (2013) 993–998, https://doi.org/10.1021/JZ400015H.
- [62] P. Dumas, S. Duguay, J. Borrel, F. Hilario, D. Blavette, Atom probe tomography quantification of carbon in silicon, Ultramicroscopy 220 (2021), 113153, https:// doi.org/10.1016/J.ULTRAMIC.2020.113153.
- [63] S.M. Reddy, D.W. Saxey, W.D.A. Rickard, D. Fougerouse, S.D. Montalvo, R. Verberne, A. van Riessen, Atom probe tomography: development and application to the geosciences, Geostand. Geoanal. Res. 44 (2020) 5–50, https:// doi.org/10.1111/GGR.12313.
- [64] A. Rossi, B. Elsener, XPS analysis of passive films on the amorphous alloy Fe70Cr10P13C7: Effect of the applied potential, Surf. Interface Anal. 18 (1992) 499–504. https://doi.org/10.1002/sia.740180708.
- [65] D. De Filippo, A. Rossi, B. Elsener, S. Virtanen, XPS analytical characterization of amorphous alloys: Fe7 Cr oP C7, Surf. INTERFACE Anal. 15 (1990) 668–674, https://doi.org/10.1002/sja.740151106.
- [66] P. Leblanc, G.S. Frankel, A Study of Corrosion and Pitting Initiation of AA2024-T3 Using Atomic Force Microscopy, J. Electrochem. Soc. 149 (2002) B239, https://doi.org/10.1149/1.1471546.
- [67] A. Ayyagari, V. Hasannaeimi, H. Arora, S. Mukherjee, Electrochemical and Friction Characteristics of Metallic Glass Composites at the Microstructural Length-scales, Sci. Rep. 2018 8:1 8 (2018) 1–10, https://doi.org/10.1038/s41598-018-19488-7.
- [68] P. Schmutz, G.S. Frankel, Characterization of AA2024–T3 by Scanning Kelvin Probe Force Microscopy, J. Electrochem. Soc. 145 (2019) 2285–2295, https://doi. org/10.1149/1.1838633.
- [69] M. Iannuzzi, K.L. Vasanth, G.S. Frankel, Unusual Correlation between SKPFM and Corrosion of Nickel Aluminum Bronzes, J. Electrochem. Soc. 164 (2017) C488–C497, https://doi.org/10.1149/2.0391709jes.
- [70] M. Rohwerder, F. Turcu, High-resolution Kelvin probe microscopy in corrosion science: Scanning Kelvin probe force microscopy (SKPFM) versus classical scanning Kelvin probe (SKP, Electrochim. Acta 53 (2007) 290–299, https://doi.org/ 10.1016/J.ELECTACTA.2007.03.016.
- [71] R. Hausbrand, M. Stratmann, M. Rohwerder, The physical meaning of electrode potentials at metal surfaces and polymer/metal interfaces: consequences for delamination, J. Electrochem. Soc. 155 (2008) C369, https://doi.org/10.1149/ 1.2926589.
- [72] R. Franke, X-ray absorption and photoelectron spectroscopy investigation of binary Nickelphosphides, Spectrochim. Acta - Part A: Mol. Biomol. Spectrosc. 53 (1997) 933–941, https://doi.org/10.1016/S1386-1425(97)00040-1.
- [73] K. Asami, H.M. Kimura, K. Hashimoto, T. Masumoto, A. Yokoyama, H. Komiyama, H. Inoue, Characterization of surfaces of amorphous Ni-Fe- P alloys, J. Non-Cryst. Solids 64 (1984) 149–161, https://doi.org/10.1016/0022-3093(84)90212-6.
- [74] A. Rossi, B. Elsener, Characterization of surface films on FeCrPC alloys by XPS and X-ray excited Auger peaks, in: P. Marcus, B. Baroux, M. Keddam (Eds.), Surface Modifications of Passive films, 12, Institute of Materials, 1994.